Title
Investigation and Suppression of Oxygen Release by LiNi0.8Co0.1Mn0.1O2 Cathode under Overcharge Conditions

Journal
Advanced Energy Materials, 12(20)

ISSN
1614-6832

Authors
Shi, Chen-Guang
Peng, Xinxing
Dai, Peng
et al.

Publication Date
2022-05-01

DOI
10.1002/aenm.202200569

Peer reviewed

Investigation and suppression of oxygen release by $LiNi_{0.8}Co_{0.1}Mn_{0.1}O_2$ cathode under overcharge conditions

Chen-Guang Shi, ‡ Xinxing Peng, ‡ Peng Dai, Penghao Xiao, Wei-Chen Zheng, Hong-Yang Li, Hang Li, Sylvio Indris, Stefan Mangold, Yu-Hao Hong, Chen-Xu Luo, Chong-Heng Shen, Yi-Min Wei, Ling Huang,* and Shi-Gang Sun**

C.-G. Shi, X. Peng, P. Dai, W.-C. Zheng, H.-Y. Li, Prof. L. Huang, Prof. S.-G. Sun
State Key Laboratory of Physical Chemistry of Solid Surfaces, Collaborative Innovation Center of Chemistry for Energy Materials, College of Chemistry and Chemical Engineering
Xiamen University
Xiamen 361005, China
E-mail: huangl@xmu.edu.cn; sgsun@xmu.edu.cn

C.-G. Shi, H. Li, S. Indris
Institute for Applied Materials
Karlsruhe Institute of Technology
Eggenstein-Leopoldshafen, 76344, Germany

X. Peng
Materials Sciences Division
Lawrence Berkeley National Laboratory
Berkeley, California 94720, USA

P. Xiao
Department of Physics & Atmospheric Science
Dalhousie University
Halifax, NS B3H 4R2, Canada

S. Mangold
Institute for Photon Science and Synchrotron Radiation
Karlsruhe Institute of Technology
Eggenstein-Leopoldshafen, 76344, Germany

Y.-H, Hong
Tan Kah Kee Innovation Laboratory (IKKEM) Center for Micro-nano Fabrication and Advanced Characterization
Xiamen, 361100, China

C.-X. Luo, Dr. C.-H. Shen, Dr. Y.-M. Wei

Contemporary Amperex Technology Co.
Ningde 352100, China
E-mail: WeiYiM@catlbattery.com

‡ These authors contributed equally to this work

Keywords: ($LiNi_{0.8}Co_{0.1}Mn_{0.1}O_2$, overcharge, oxygen release, structural change, microcracks, single-crystalline)

The safety issue of lithium-ion batteries is a crucial factor limiting their large-scale application. Therefore, it is of practical significance to evaluate the impact of their overcharge behavior because of the severe level of oxygen release of cathode materials during this abusive process. Herein, by combining a variety of in situ techniques of spectroscopy and electron microscopy, we studied the structural degradation of $LiNi_{0.8}Co_{0.1}Mn_{0.1}O_2$ (NCM811) accompanying the oxygen release in the overcharge process. We observed that a small amount of O_2 evolved from the initial surface at ~4.7 V. When charging to a higher voltage (~5.5 V), a large amount of O_2 evolved on the newly formed surface due to microcracks occurrence. Based on experimental results and theoretical calculations, we determined that the oxygen release mainly occurs in the near-surface regions, where the remaining oxygen vacancies accumulate to create voids. To suppress the oxygen release, single-crystalline NCM811 with integrated structure was introduced and served as cathode, which can effectively inhibit morphology destruction and reduce the activation of lattice oxygen in the surface region. Our findings provide a theoretical basis and effective strategy for improving the safety performance of Ni-rich cathode materials in practical applications.

1. Introduction

Recently, considerable efforts have been devoted to the development of lithium-ion batteries, and the main focus consists in the energy density of the battery.[1,2] However,

the safety performance of a battery is another important factor limiting its final commercialization.[3-5] Therefore, evaluation of the battery function under harsh conditions is critical.[6-8] The safety issues mainly involve thermal runaway, which is considered to be closely related to battery overcharge.[6,9] Severe structural change in the overcharge process has been reported as it is accompanied by heat release and gas evolution.[10-12] Because of the combustion-supporting properties of O_2, its presence will lead to an explosion under a thermal-runaway situation, causing serious safety hazards.[13,14] Therefore, further investigation of the oxygen-release behavior under overcharge is essential.

Ni-rich cathode materials ($LiNi_xCo_yMn_{1-x-y}O_2$, x>0.5, NCM for short) have received widespread attention because of their high specific capacity and low cost.[15,16] The main issue concerns their inferior cycling performance, especially under the overcharge condition.[17,18] Some studies have attributed the failure mechanism to the unstable interphase components and microcracks formation.[19-21] Other studies have focused on the oxygen-release behavior and the accompanying structural transformation from the original layered phase to a disordered spinel and/or rock-salt phase.[22-24] Working under high-current conditions would only exacerbate this negative effect, because of the heterogeneity of the Li and transition metals (TM) distribution,[25] which could destroy structural ordering and result in interfacial deterioration.[23,26,27] Therefore, researchers have mainly regarded the root cause to be excess oxidation of TM at high voltage and have seldom explored the property of the oxygen species, which also shows high activity due to strong TM–O covalence.[28,29]

In addition, the region associated with oxygen release and evolution remains ambiguous. Most researchers believe that this phenomenon mainly occurs at the surface, [30,31] but under some extreme conditions, O_2 may also be trapped in the inner bulk,[14] which has led to continued debate over the specific mechanism. First, researchers have mainly focused on the cumulative gas evolution after many cycles or at elevated temperature conditions, but have rarely explored the relationship between oxygen release and gas evolution during a single cycle. [32,33] In fact, when charging to a higher voltage, especially under overcharge conditions, a multitude of reactive oxygen species will appear conspicuously and O_2 will even evolve.[31,34-36] Second, in terms of the analysis of the structural change during the electrochemical process, only some regional measurements that are limited to a certain length scale have been performed, where the local structures of oxygen release are not detected. It is also challenging to employ in situ techniques, resulting in the real-time reaction details remaining ambiguous, especially for the active region and diffusion mode of oxygen. [37,38] Furthermore, it is mainly believed that the structural transformation is closely correlated with oxygen release.[10,39] However, the origin of the material decay is not clear, especially under some extreme conditions, which is mainly regarded as a coupling effect by electrochemical polarization, mechanical effects, thermal effects, etc.[12,14,40]

In this work, we have carried out the multi-scale analysis of NCM811 under overcharge conditions that simulate the process of a sudden high current causing a sharp voltage rise in the battery. A variety of diffraction and spectroscopic techniques

was employed to investigate this abusive process, including in situ X-ray diffraction (XRD), in situ Raman, ex situ solid-state nuclear magnetic resonance spectroscopy (ss-NMR), ex situ X-ray absorption spectroscopy (XAS) and combined with the ^{18}O labelling method using online electrochemical mass spectrometry (OEMS). From our results, we performed a quantitative analysis of the labelled ^{18}O, which can be perceived as distributed in the surface region. The evolved O_2 is mainly composed of ^{18}O for the early overcharge stage and ^{16}O for the later overcharge stage, indicating oxygen release happened in the surface and bulk, respectively. However, no obvious structural change occurred in the bulk according to spectroscopic analysis. Using SEM, TEM, and other local structure characterization techniques, the phase-transition components appear near the surface at the nanoscale. Furthermore, the main reason for oxygen release is revealed as that at the ultrahigh voltage for these conventional polycrystalline materials apparent intergranular and intragranular cracks will appear simultaneously, which would expose a vast fresh surface inside secondary particle. Because of the higher activity of lattice oxygen in the vicinity of the outer layers for separated primary particles, the oxygen-release behavior could be greatly aggravated under such an abusive condition. In view of this, we propose an effective strategy by using single-crystalline NCM811 (SC-NCM811). The SC-NCM811 with fewer grain boundaries and more integrated crystalline structures have greatly reduced oxygen release during the overcharge process. Our proposed mechanism and corresponding strategy provide a solution to reduce the potential safety hazards for practical applications of Ni-rich cathode materials.

2. Results and Discussion

2.1 Experiment setup and quantification of oxygen release in overcharge process

Polycrystalline Ni-rich cathode material was employed as the subject of our study. Figure 1a presents an SEM image of commercial polycrystalline NCM811. Its morphology consists of spherical secondary particles formed by the agglomeration of primary particles. Figure S1 shows that the size of the secondary particles is mainly concentrated in the range of 3–10 μm, and the primary particles are hundreds of nanometers in size. A powder XRD scan of pristine NCM811 is presented in Figure 1b. The ratio of the (003)/(104) peaks exceeds 1.2, and the (006)/(102), (108)/(110) peaks present obvious splitting phenomena, which are typical characteristics of the layered structure; [41,42] a schematic diagram of the crystal structure is illustrated in Figure 1c, with alternating LiO_6 and TMO_6 layers.[43] This material exhibits excellent electrochemical performance under normal working voltage, as shown in Figure S2. For the first formation cycle, it delivers a discharge capacity of 212.9 mAh g^{-1} at 0.1 C with a cutoff voltage of 4.3 V and 196.7 mAh g^{-1} at 0.2 C. The cyclic retention for 50 cycles is 90.2%, indicating good cyclic performance. Excellent rate capability was also observed, indicating good kinetic stability. In this work, we mainly explore the structural/morphological change and the mechanism of oxygen release during the overcharge process and propose a modification method on this basis.

The overcharge behavior was examined under conditions of a large charge rate of 1C (1 C = 200 mAh g^{-1}) for 2 h. The specific charging and discharging procedures are cycled at 0.2 C in the voltage range of 2.8–4.3 V and then adjust the charging

condition to 1 C for 2 h, and later, the subsequent discharge and charge result in a return to the previous state. Figure 1d presents the charge–discharge curves according to the overcharge program, with the red line corresponding to the overcharge process. As observed in the overcharge curve, the maximum voltage reached ~5.5 V when charging 1.5 h and was maintained until the end of the overcharge, with good repeatability as shown in Figure S3. Note that the plateau (~5.5 V) appeared due to electrolyte oxidation. The actual capacity (400 mAh g^{-1}) is much higher than the theoretical capacity (~273 mAh g^{-1}) assuming all Li is extracted from the bulk. [17] After the overcharge process, an obvious irreversible capacity loss of 18.2% occurred in comparison with that of the most recent cycle performance before overcharging (157.6 vs. 192.6 mAh g^{-1}). The capacity loss indicates that the overcharge will cause, in addition to electrolyte decomposition, electrochemical degradation of NCM811, including interphase impedance increase (Figure S4a), the cycling performance (Figure S4b) and the rate capability (Figure S4c) deteriorated after the overcharge process. As only one-time overcharge behavior could impose a great negative effect on the battery, it is necessary to combine several techniques to enable multiscale exploration of the failure mechanism during this overcharge process.

First, we have concerned about the gas evolution, which directly affects the safety performance of the whole battery. As shown in Figure 1e, a large amount of O_2 evolved during the overcharge process (see Figure S5). Importantly, the oxygen element in O_2 completely originated from the cathode structural lattice. However, the identification of the oxygen-release region remains unknown.[12,35] Herein, the isotope

^{18}O was employed thus to mark the near-surface region using a thermal treatment,[44-46] which was confirmed by Time of Flight Secondary Ion Mass Spectrometry (TOF-SIMS) results in Figure S6. This method can distinguish whether the source region of oxygen release is at the near-surface or inside the inner particle. OEMS analysis was performed to determine the amount of gas evolved inside the battery during the overcharge process. The flow rate along the overcharge process is shown in Figure 1e, where m/z=32, 34 and 36 correspond to $^{16}O^{16}O$, $^{16}O^{18}O$ and $^{18}O^{18}O$ molecules, respectively. Based on the m/z of O_2, the oxygen-release region in different overcharge stages could be clearly detected. Less O_2 evolved in the early stage of overcharge (~4.7 V). When charging to a higher voltage (~5.5 V), a large amount of O_2 appeared. By combining the changes in O_2 evolution and the overcharge curve, we divided this process into three stages: I. below the normal cutoff voltage (4.3 V), there was no oxygen evolved in this stage; II. a small amount of O_2 evolved, corresponding to 4.3–5.5 V; and III. a large amount of O_2 appeared and the evolution rate distinctly increased to a high value for m/z=32, 34 and 36, relating to the overcharge plateau at ~5.5 V. Some other electrochemical parameters in selected states were presented in Table S1, and the specific O_2 evolution data were listed in Table S2. In stage II, $^{16}O^{18}O$ (52.46%) and $^{18}O^{18}O$ (30.87%) are the dominant oxygen species, which is closely correlated to the initial surficial labeling ^{18}O of the secondary particles. In stage III, $^{16}O^{16}O$ (40.64%) and $^{16}O^{18}O$ (40.89%) become the major constituents, suggesting that inner oxygen is involved in oxygen release. However, there are two aspects for the inner oxygen release, one is from the bulk, and the other is from the grain boundaries.

Basically, we considered drastic structural change is going to occur in this harsh condition. In order to figure out the mechanism of oxygen release, we first carry out in situ and ex situ techniques of spectroscopy to investigate the failure mechanism.

2.2 Revealing bulk-structure evolution using ex situ and in situ techniques

Multiple ex situ and in situ diffraction and spectroscopy techniques were used to explore the structural change in NCM811. Figure S7a presents in situ XRD scans for the full degree range, showing the drastic change for each diffraction peak, including peak shift and changes in the intensity and profile type. Figure 2a demonstrates the change of (003) diffraction peak of NCM811 during the overcharge process. There is a small negative shift (from 18.67° to 18.30°) in stage I. In stage II, the most obvious change is a large positive shift from 18.30° to 19.98°, an intensity decrease, and peak widening. Almost no change occurred in stage III (from 20.03° to 20.06°), which appears to contradict the OEMS result. Other diffraction peaks (Figure S7b–c) also illustrated the same tendency as the (003) peak, indicating the largest structural change. Among them, the structural change along the (003) crystal plane showed the largest variation especially during Stage II, in accordance with the diffusion path of lithium ions, which can be regarded as phase transformation from O3 to O1 in the bulk.[10,47,48]

Figure 2b provides the cell parameters a, c and the unit cell volume V determined by Rietveld refinement during the overcharge process. They all show major variation in stage II (Δc=6.85%, Δa=1.72%, ΔV=10.03%), indicating structural change along the c-axis, which can be attributed to TM further oxidation and excessive Li extraction at

this time.[49] In contrast, the parameters remained steady in stage III. For stages I and II, massive lithium removal from the cathode leads to a strong structural change. However, no obvious phase transition occurred in stage III; that is, the layered phase does not transform into the spinel or rock-salt phase, mainly because bulk-sensitive XRD only reflects the average information for structural changes, and a small amount of phase transition components could not be detected.

Raman spectroscopy mainly detects the atomic vibration for the selected secondary particle, and the Raman activity depends on the symmetry of the local near-surface structure.[50] Figure 2c presents Raman spectra of NCM811 during the overcharge process, where the two peaks are the E_g and A_{1g} modes distinguished mainly by oxygen motions.[51] Before the overcharge process, a wide peak was observed. It then gradually splits into two peaks (at ~ 480 cm^{-1} and ~ 555 cm^{-1}) after stage I owing to Li extraction and TM oxidation, especially the emergence of Ni^{4+} that could increase the covalence of the Ni–O bond and enhance the peak intensity. In stage II, these two peaks exhibited the largest change in amplitude, corresponding perfectly to the XRD results. The E_g peak shows blue shift by ~11 cm^{-1}, and the intensity decreased; while A_{1g} appears red shift by ~2 cm^{-1}, and the intensity also decreased. These results indicate that the chemical environment around TM changed greatly, affected not only by TM oxidation but also by the oxygen oxidation or release. However, in stage III, these two peaks only occurred a small decrease in intensity, regardless of the fluorescence effect, for which detailed information is provided in Figure S8. It can be assumed that the chemical environment surrounding TM does not change substantially

in stage III, which also proves that the oxygen vacancies are unlikely to diffuse gradually from the surface to the interior of the secondary particles. Therefore, it is of high probability that oxygen release from localized regions inside the particles plays a pivotal agent during the overcharge process.

ss-NMR can provide local structural information on specific elements such as Li in materials, such as the Li content and coordination environment.[15,52] Figure 2d presents the ^{7}Li solid-state NMR spectra of NCM811 at different stages. In fact, some Li^{+} remained trapped in the bulk, as indicated by the observed weak signal (~250 ppm for the red line) after the overcharge process. The broad peaks (from 1000 to 0 ppm) in the pristine state can be attributed to the Li^{+} surrounded by $Ni^{2+}/Ni^{3+}/Mn^{4+}$ next nearest neighbors.[53] After stage II, the lithium content in the bulk dropped to a very low level (~9%), indicating that most of the lithium extraction has been completed, which also reflects the huge structural change in stage II. After stage III, this part of Li (~9%) still remained within the bulk, showing no obvious change compared with that of stage II. It can be considered further that most of the TM near the remaining Li is Ni^{4+}, indicating that the TM in the bulk maintains a higher valence state. Comparing the peak positions of stage II and III, no significant change in the chemical-coordination environment near Li in stage III was observed, indicating that the ultrahigh-voltage state cannot further extract the lithium trapped in the bulk, and no obvious change around the Li chemical environment occurs.

To eliminate the probability of lower resolution, high-energy synchrotron radiation technology was used to analyze the TM oxidation state.[54,55] Figure 2e presents the X-

ray absorption near-edge structure (XANES) diagrams of the Ni, Co, and Mn K-edges in different overcharge stages of NCM811. For stages I and II, all the spectral peaks shifted substantially, indicating the valence-state change at this time. In stage I, the oxidation of Ni was related to lithium extraction. In stage II, all of the Ni, Co, and Mn underwent a certain valence increase, corresponding to the drastic structural change in the bulk at this time. Similarly, in stage III, the Co and Mn valence basically remained constant, whereas the Ni spectrum showed a negative shift, demonstrating that there is only a reduction tendency of Ni and no more TM oxidation. This phenomenon strongly correlates to Li/Ni mixing in the surface because many Li vacancies appeared at this high voltage. Moreover, it could be also related to loss of oxygen accompanied by the formation of Ni-rich rock-salt phases.

In general, these spectroscopic characterization results describe a tremendous structural change occurring in stage II, which resulted from excess Li extraction and TM oxidation. In contrast, there was no obvious structural change in the ultrahigh voltage state in stage III. This seems to be conflicting with the massive O_2 evolution, which can basically rule out the oxygen release from the bulk or the surface of secondary particles. However, the minor valence change of the TM could explain this severe change thanks to the high resolution, and this change occurs heterogeneously in some regions. Precluding that the bulk is the source of structural degradation, we speculate that structural degradation occurs in the grain boundaries from the internal local regions.

2.3 Characterization of local structures using electron microscopy

Figure 3a presents cross-sectional SEM images of NCM811 during the overcharge process. It can be seen that new cracks formed inside the secondary particles, and the cracks gradually grew and propagated. More specifically, there was nearly no crack formation during stage I, indicating better morphological stability below 4.3 V, which is also consistent with good cyclic performance in the voltage range of 2.8-4.3 V. During stage II, a few cracks began to appear within the secondary particles at ~4.7 V. Afterwards, the internal cracks extended to the surface, and more cracks were observed in the SEM images. Notably, the occurrence and propagation of cracks were remarkably increased compared with those in stages I and II, and the intact morphology of the secondary particles was severely damaged after stage III. We characterized NCM811 using high-angle annular dark-field scanning transmission electron microscopy (HAADF-STEM) after stage III, as shown in Figure 3b. The low-magnification STEM image illustrates that the diameters of many particles were only a few hundred nanometers or even smaller. This finding indicates that the formation of intergranular cracks completely destroys the overall structure of the secondary particles. In addition to the intergranular cracks between particles, intragranular cracks were also observed within the primary particles. The STEM results of NCM811 at different overcharge stages show that the secondary spherical particles would first be broken into aggregates of the primary particles randomly and then further separated into individual primary particles, see Figure S9. Figure 3c displays a representative HAADF-STEM image of an NCM811 nanoparticle with intragranular cracks and the

corresponding element mappings of Ni, Co, Mn, and O after stage III, also see Figure S10. The STEM-EDS mapping confirms the uniform distribution of Ni, Co, Mn, and O within the primary particle. Therefore, we hypothesize that the crystalline structure of primary particles has not changed during the overcharge process. To better understand the detailed structure progression during the overcharge process, aberration-corrected STEM was then conducted to image particles after overcharging. After stage III, primary particles appeared to be "sliced" in parallel along the (003) plane, indicating a mode of in-plane shear cracking in fracture mechanics (Figure 3d). Furthermore, some small cracks indicate a mode of opening fracture is also found at the surface of the primary particles (Figure 3e-f). Of note, rocksalt components were discovered near the initial surface region and newly formed surface, as shown in Figures 3e, S11, and S12. There are small pore structures left attributed to the release of lattice oxygen in the region, where the rocksalt components are formed (Figure S12c). Interestingly, rocksalt components not only appeared along the lithium diffusion channel (see Figure 3f), but also on the surface perpendicular to the channel (see Figure 3g). The phase transition only occurs at the depth of several atomic layers from the surface to the bulk, and it cannot contribute to the total O_2 evolution solely as estimated from results (0.6754 $m^2 g^{-1}$). In summary, during the overcharge process, the source of oxygen is mainly the surface of the particles, including the new fresh surface exposed by the rupture of the morphology of the secondary particles.

2.4 Discussion

On the basis of the above results, we proposed the failure mechanism of NCM811 and observed that the origin of the oxygen release could be separated into two steps. For stage II, the TM excess oxidation helps to increase the amount of active oxygen species due to the strong covalence of the TM–O band. However, this step possibly only occurs on the surface of secondary particles because of the observed intact morphology nearly remaining after this stage. For stage III in the ~5.5 V plateau, many Li vacancies will accumulate great internal micro-stress, lattice surface oxygen would suddenly release and the O_2 evolution rate drastically increases due to the occurrence and propagation of intergranular and intragranular cracks. Note that oxygen release regions mainly include the fresh surface exposed by the destruction of the morphology of the secondary particles. So, the essential difference between these two oxygen release actions in Stage II and III is the active oxygen atoms in different regions. The surface oxygen of the secondary particle was easily oxidized because of the many Li vacancies in the early stage of overcharge. Then, the oxygen between the grain boundaries started to oxidize caused by the elevated voltage and inferior mechanical properties. The oxygen-release behavior impels phase transformation and leaving many voids, which aggravated impedance at the interphase and affected the electrochemical performance. Moreover, O_2 evolution will increase the internal pressure of the battery, and the combustion-supporting performance will accelerate the process of thermal runaway, which brings severe safety hazards. In view of this, we regard the effective strategy of lower grain boundaries morphology, which is helpful to inhibit the degree of oxygen release.

A feasible approach for stabilizing NMC811 is to introduce single-crystalline materials with reduced grain boundaries, limited surface, and a more integrated crystalline structure.[56,57] Figure S13 presents an XRD pattern and SEM image of this single-crystalline NCM811 (SC-NCM811). The XRD pattern indicates a similar layered structure as that of the poly-crystalline NCM811 (PC-NCM811) described above, and the SEM image shows that the particle sizes are a few micrometers without agglomeration morphology. The corresponding TEM image and electron diffraction patterns viewing along [001] direction of SC-NCM811 is illustrated in Figures 4a and 4b, indicating its well single-crystal characteristic. Li/SC-NCM811 batteries also exhibited excellent cycling performance and rate capability in normal conditions, as shown in Figure S14. Figure 4c displays the oxygen release during the same overcharge process for the Li/SC-NCM811 battery, where the ^{18}O isotope also labelled the surface of SC-NCM811 by the same method and confirmed by TOF-SIMS in Figure S15. The O_2 evolution was greatly suppressed on SC-NCM811, whether it was the gas amount or rate during the whole overcharge process. When charging to stage II, the content of O_2 fragments for m/z=32, 34, and 36 of SC-NCM811 are cut down distinctly, indicating that the oxygen activity on the surface was reduced. For the m/z=32 fragment in Stage III, oxygen from the inner structure also showed a decreased tendency, indicating that without agglomeration morphology and fewer grain boundaries, less fresh surface would be exposed. In addition, this assumption can be confirmed by the HADDF-STEM image in Figure 4d, which was obtained after the overcharge process, showing that its morphology was intact with less destruction,

and the element distribution remained uniform (see Figure S16). The cycling performance of Li/SC-NCM811 and Li/PC-NCM811 batteries is shown in Figure 4e; the results indicate that the SC-NCM811 can drastically reduce the capacity decay after the overcharge process; see also Figures S4 and S17. Figure 4f presents EIS data of the batteries before and after overcharge, which illustrates that the SC-NCM811 could effectively prevent an impedance increase after the overcharge process. Therefore, from the experimental results, we know that the surface degradation of the particles accounted for the failure, and the reduced amount of boundaries in the SC-NCM811 greatly inhibits oxygen release phenomenon.

Combined with DFT calculations, it can be concluded that oxygen release mainly occurs in the near-surface regions. Even though the bulk transition of $NiO_2 \rightarrow NiO + 0.5O_2$ has a large thermodynamic driving force, the whole structure cannot collapse and release all O_2 at the same time. O vacancy must form as the first step, either staying on the surface or diffusing into the bulk. A corresponding schematic graph for $Li_{0.0}NiO_2$ is illustrated in Figure 4g. The O vacancy formation energy (E_{vo}) is highly positive in bulk Li_xNiO_2 from our DFT calculations. At x=0.5, E_{vo}=2.27 eV; at x=0.25, E_{vo}=1.78 eV and 2.13 eV for two distinct sites; at x=0, E_{vo} is still 2.33 eV. These numbers suggest that the solubility of an O vacancy in the bulk is lower than 5×10^{-31} mole fraction at room temperature. The diffusion barrier (E_a) is also very high in the bulk, ranging from 1.89 eV at x=0.5 to 2.65 eV at x=0.0. Therefore, the O vacancy is unlikely to migrate to the bulk of Ni-rich oxides from both thermodynamic and kinetic perspectives. In contrast, the energy of O_2 gas formation (generate two O vacancies)

on the surface was only 0.54 eV at x=0 and 1.42 eV at x=0.25. Considering the entropy change, O_2 evolution in the surface at x=0 is highly feasible. In addition, this surface includes the grain boundaries from the inner region at the high voltage, which are likely to develop into newly exposed surface. Therefore, we can draw a conclusion that oxygen release indeed occurs in the particle surface rather than migrating into bulk in this overcharge process. On top of this, the SC-NCM811 with fewer grain boundaries shows lower oxygen activity than that of the PC-NCM811, which could enhance the safety performance of Ni-rich cathodes.

3. Conclusion

The ^{18}O isotope DEMS method allows not only tracking the gas evolution but also distinguishing the source regions, i.e. in the internal or surface region for secondary particles. By coupling a variety of in situ and ex situ diffraction, spectroscopic, and advanced electron microscopic techniques, the decay of NCM811 batteries at overcharge conditions can be attributed to oxygen release, which mainly happens in the near-surface regions and creates voids. For conventional polycrystalline NCM811, great structural change will lead to intergranular and intragranular cracks inevitably occurring and propagating at a high-voltage state. This would leave an inner fresh surface exposed to the electrolyte, and the evolved O_2 would bring serious safety hazards. To address this problem, the single-crystalline NCM811 with fewer grain boundaries could greatly reduce oxygen release. It demonstrates a relatively stable structure and complete morphology by minimizing the amount of reactive oxygen

species. Our results provide the failure mechanism during the overcharge process and the corresponding effective strategy that could significantly enhance Ni-rich cathode materials' safety performance in the practical use.

4. Experimental Section

Sample preparation: Polycrystalline and single-crystalline $LiNi_{0.8}Co_{0.1}Mn_{0.1}O_2$ cathode materials were provided by CATL (Contemporary Amperex Technology Co., Limited, Ningde, China). The isotope ^{18}O was labelled on the near-surface of NCM811 by thermal treatment. To be specific, NCM811 was put in the tube furnace with the $^{18}O_2$ gas inside. The heating procedure was 500 °C for 6 h, which was lower than the actual calcine temperature. This could help labelled the surface oxygen species and prevent over oxidation. The active material, acetylene black and PVDF were dissolved in NMP with a mass ratio of 90:5:5, then they were mixed evenly and coated on aluminum foils and stainless steel plates with a thickness of 150 μm, and heated at 110 °C overnight under vacuum. The dry electrodes were cut into round pieces, and pressed at 5 MPa (Φ12.7mm, with ~10 mg cm^{-2} loading weight). Lithium metal foil (Φ16 mm, 2 mm thickness, DoDoChem) was chosen as anode, PP (Celgard 2400) and glassfiber (Whatman) was chosen as separator. Electrolyte composition is 1M $LiPF_6$ lithium salt dissolved in EC/EMC = 3/7 w/w solvent (DoDoChem). When assembling the battery in 2025-type coin cells, H_2O and O_2 content in the glovebox are both controlled less than 5 ppm. As for removing the cathode electrodes after the electrochemical reactions, they were rinsed with DMC for three times and stored in the glovebox.

Electrochemical measurements: After assembling the battery and storing it for 6 hours, the electrochemical measurement was carried out. Sealed coin cells were generally tested at 0.2 C (1 C = 200 mAh g^{-1}) for charge-discharge processes within the voltage range 2.8-4.3 V at 25°C. For the overcharge behavior, the charging condition was set to 1 C for 2 h during the 6th cycle, and for the subsequent cycle the rate was set to 0.2 C again within 2.8-4.3 V. For in situ measurement, a formation

process is generally cycled at 0.2 C first, then the overcharge process is performed. The electrochemical measurements were generally carried out on Neware Software and EC-LAB. The LSV test was carried out on the CHI600 instrument, with the sweep speed at 1mV s^{-1}. Gas evolution of the battery is analyzed by OEMS (modified 5975C mass-selective detector, Agilent). The carrier gas is He, and the flow rate was 5 ml min^{-1}.

Materials characterization: The morphology of the samples is mainly characterized by SEM (Hitachi S-4800). The specific surface area was obtained by BET test (Micromeritics ASAP2460, USA). The phase analysis was performed by XRD (Bruker D8, Germany) with Cu Kα1 radiation, and the test condition was 40 kV and 40 mA. For ex situ XRD, the scan speed was 2° min^{-1} within the range of 15-72°. For in situ XRD, each scan lasted 5 min, and the window of the electrolytic cell was selected as Be. The crystallographic parameters were obtained through TOPAS4.2 software by Rietveld method. In situ Raman was measured on Renishaw (UK). The laser wavelength was 632.8 nm, the power was 1 mW, and the window of in situ electrolytic cell was made of quartz. Each spectrum was collected within 450 s, and the spectrum range was 300-800 cm^{-1}. The local Li environment was investigated by magic-angle spinning (MAS) ^{7}Li solid-state nuclear magnetic resonance spectroscopy (Bruker Avance neo) at the field of 4.7 T, corresponding to a resonance frequency of 77.8 MHz. Spinning was performed in 1.3 mm rotors at 60 kHz. The valence state of transition metals was characterized by X-ray absorption spectroscopy at XAS beamline (ANKA, KIT). TEM, HAADF-STEM, EDS for NCM811 were conducted using an aberration-corrected electron microscope (TEAM 1 and ThemIS) operated at 300 kV at the National Center for Electron microscopy of Lawrence Berkeley National Laboratory.

Computational methods: All DFT calculations were performed with the Vienna Ab initio Simulation Package (VASP). The valance electrons were described by the plane wave basis set with an energy cutoff of 520 eV. The core electrons were incorporated by the projector augmented wave method (PAW) method. The exchange correlation

term is accounted by the strongly constrained and appropriately normed (SCAN) density functional. The O vacancy formation energy is defined as:

E_{vo}=E(M-O) + ½*E(O_2)-E(M)

where M-O is the structure with one O vacancy and M is the one without.

Supporting Information

Supporting Information is available from the Wiley Online Library or from the author.

Acknowledgements

This work was jointly supported by the National Natural Science Foundation of China (Grants 22172133 and 21673194), and the National Key Research and Development Program of China (2016YFB0100202). Work at the Molecular Foundry was supported by the Office of Science, Office of Basic Energy Sciences, of the U.S. Department of Energy under Contract No. DE-AC02-05CH11231.

References

[1] Y. Cao, M. Li, J. Lu, J. Liu and K. Amine, *Nat. Nanotechnology*, **2019**, 14, 200.

[2] X. Wang, Y. L. Ding, Y. P. Deng and Z. Chen, *Adv. Energy Mater.*, **2020**, 10, 1903864.

[3] A. Li, A. C. Y. Yuen, W. Wang, I. M. De Cachinho Cordeiro, C. Wang, T. B. Y. Chen, J. Zhang, Q. N. Chan and G. H. Yeoh, *Molecules* **2021**, 26, 478.

[4] L. Zhang, X. Li, M. Yang and W. Chen, *Energy Storage Mater.* **2021**, 41, 522.

[5] T. Ould Ely, D. Kamzabek and D. Chakraborty, *Front.Energy Res.* **2019**, 7, 71.

[6] K. Liu, Y. Liu, D. Lin, A. Pei, and Y. Cui, Sci. Adv., **2018**, 4, eaas9820.

[7] X. Zeng, M. Li, D. Abd El-Hady, W. Alshitari, A.S. Al-Bogami, J. Lu and K. Amine, *Adv. Energy Mater.*, **2019**, 9, 1900161.

[8] L.-J. Li, Z.-D. Zhu, J. Dai, R.-R Wang, and W. Peng, *J. Electrochem*, **2021**, 27, 405.

[9]D. Ren, X. Feng, L. Liu, H. Hsu, L. Lu, L. Wang, X. He and M. Ouyang, *Energy Storage Mater.*, **2021**, 34, 563.

[10]C. Xu, P.J. Reeves, Q. Jacquet and C. P. Grey, *Adv. Energy Mater.*, 2020, 11, 2003404.

[11]K.-W. Nam, S.-M. Bak, E. Hu, X. Yu, Y. Zhou, X. Wang, L. Wu, Y. Zhu, K.-Y. Chung and X.-Q. Yang, *Adv. Funct. Mater.*, **2013**, 23, 1047.

[12]S. Sharifi-Asl, J. Lu, K. Amine and R. Shahbazian-Yassar, *Adv. Energy Mater.*, **2019**, 9, 1900551.

[13] Q. Wang, P. Ping, X. Zhao, G. Chu, J. Sun and C. Chen, *J. Power Sources*, **2012**, 208, 210.

[14] P. Yan, J. Zheng, T. Chen, L. Luo, Y. Jiang, K. Wang, M. Sui, J. G. Zhang, S. Zhang and C. Wang, *Nat. Commun.*, **2018**, 9, 2437.

[15] C. Xu, K. Märker, J. Lee, A. Mahadevegowda, P. J. Reeves, S. J. Day, M. F. Groh, S. P. Emge, C. Ducati, B. Layla Mehdi, C. C. Tang and C. P. Grey, *Nat. Mater.*, **2021**, 20, 84.

[16] W. Li, E. M. Erickson and A. Manthiram, *Nat. Energy*, **2020**, 5, 26.

[17] S.-T. Myung, F. Maglia, K.-J. Park, C. S. Yoon, P. Lamp, S.-J. Kim and Y.-K. Sun, *ACS Energy Lett.*, **2016**, 2, 196.

[18] L. de Biasi, B. Schwarz, T. Brezesinski, P. Hartmann, J. Janek and H. Ehrenberg, *Adv. Mater.*, **2019**, 31, 1900985.

[19] G. W. Nam, N.-Y. Park, K.-J. Park, J. Yang, J. Liu, C. S. Yoon and Y.-K. Sun, *ACS Energy Lett.*, **2019**, 4, 2995.

[20] H. Liu, M. Wolf, K. Karki, Y. S. Yu, E. A. Stach, J. Cabana, K. W. Chapman and P. J. Chupas, *Nano Lett.*, **2017**, 17, 3452.

[21] Z. W. Lebens-Higgins, S. Sallis, N. V. Faenza, F. Badway, N. Pereira, D. M. Halat, M. Wahila, C. Schlueter, T.-L. Lee, W. Yang, C. P. Grey, G. G. Amatucci and L. F. J. Piper, *Chem. Mater.*, **2018**, 30, 958.

[22] S.-K. Jung, H. Gwon, J. Hong, K.-Y. Park, D.-H. Seo, H. Kim, J. Hyun, W. Yang and K. Kang, *Adv. Energy Mater.*, **2014**, 4, 1300787.

[23] L. Zou, W. Zhao, Z. Liu, H. Jia, J. Zheng, G. Wang, Y. Yang, J.-G. Zhang and C. Wang, *ACS Energy Lett.*, **2018**, 3, 2433.

[24] S. Lee, W. Jin, S. H. Kim, S. H. Joo, G. Nam, P. Oh, Y.-K. Kim, S. K. Kwak and J. Cho, *Angew. Chem. Int. Ed.*, **2019**, 58, 2.

[25] H. Hyun, K. Jeong, H. Hong, S. Seo, B. Koo, D. Lee, S. Choi, S. Jo, K. Jung, H. H. Cho, H. N. Han, T. J. Shin and J. Lim, *Adv. Mater.* **2021**, 33, e2105337.

[26] Y.-N. Zhou, J.-L. Yue, E. Hu, H. Li, L. Gu, K.-W. Nam, S.-M. Bak, X. Yu, J. Liu, J. Bai, E. Dooryhee, Z.-W. Fu and X.-Q. Yang, *Adv. Energy Mater.*, **2016**, 6, 1600597.

[27] S. Hwang, E. Jo, K. Y. Chung, K. S. Hwang, S. M. Kim and W. Chang, *J. Phys. Chem. Lett.*, **2017**, 8, 5758.

[28] Q. Chen, Y. Pei, H. Chen, Y. Song, L. Zhen, C. Y. Xu, P. Xiao and G. Henkelman, *Nat. Commun.*, **2020**, 11, 3411.

[29] G. Cherkashinin, M. Motzko, N. Schulz, T. Späth and W. Jaegermann, *Chem. Mater.*, **2015**, 27, 2875.

[30] F. Lin, I. M. Markus, D. Nordlund, T. C. Weng, M. D. Asta, H. L. Xin and M. M. Doeff, *Nat. Commun.*, **2014**, 5, 3529.

[31] R. Jung, M. Metzger, F. Maglia, C. Stinner and H. A. Gasteiger, *J. Electrochem. Soc.*, **2017**, 164, A1361.

[32] C. H. Jung, D. H. Kim, D. Eum, K. H. Kim, J. Choi, J. Lee, H. H. Kim, K. Kang and S. H. Hong, *Adv. Funct. Mater.* **2021**, 31, 2010095.

[33] J. Liu, Z. Du, X. Wang, S. Tan, X. Wu, L. Geng, B. Song, P.-H. Chien, S. M. Everett and E. Hu, *Energy Environ. Sci.* **2021**, 14, 6441.

[34] J. Li, A.R. Cameron, H. Li, S. Glazier, D. Xiong, M. Chatzidakis, J. Allen, G. A. Botton and J. R. Dahn, *J. Electrochem. Soc.*, **2017**, 164, A1534.

[35] L. Mu, R. Lin, R. Xu, L. Han, S. Xia, D. Sokaras, J. D. Steiner, T. C. Weng, D. Nordlund, M. M. Doeff, Y. Liu, K. Zhao, H. L. Xin and F. Lin, *Nano Lett.*, **2018**, 18, 3241.

[36] X. Liu, G. L. Xu, L. Yin, I. Hwang, Y. Li, L. Lu, W. Xu, X. Zhang, Y. Chen, Y. Ren, C. J. Sun, Z. Chen, M. Ouyang and K. Amine, *J. Am. Chem. Soc.*, **2020**, 142, 19745.

[37] J. Lu, T. Wu and K. Amine, *Nat. Energy*, **2017**, 2, 17011.

[38] D. Wang, C. Xin, M. Zhang, J. Bai, J. Zheng, R. Kou, J. Y. Peter Ko, A. Huq, G. Zhong, C.-J. Sun, Y. Yang, Z. Chen, Y. Xiao, K. Amine, F. Pan and F. Wang, *Chem. Mater.*, **2019**, 31, 2731.

[39] X. Zeng, C. Zhan, J. Lu and K. Amine, Chem, 2018, 4, 690-704.

[40] G. L. Xu, X. Liu, A. Daali, R. Amine, Z. Chen and K. Amine, *Adv. Funct. Mater.*, **2020**, 30, 2004748.

[41] Z. Wu, S. Ji, J. Zheng, Z. Hu, S. Xiao, Y. Wei, Z. Zhuo, Y. Lin, W. Yang, K. Xu, K. Amine and F. Pan, *Nano Lett.* **2015**, 15, 5590.

[42] S. Cui, Y. Wei, T. Liu, W. Deng, Z. Hu, Y. Su, H. Li, M. Li, H. Guo, Y. Duan, W. Wang, M. Rao, J. Zheng, X. Wang and F. Pan, *Adv. Energy Mater.* **2016**, 6, 1501309.

[43] H.-H. Ryu, B. Namkoong, J.-H. Kim, I. Belharouak, C. S. Yoon and Y.-K. Sun, *ACS Energy Lett.*, **2021**, 6, 2726.

[44] S. E. Renfrew and B. D. McCloskey, *J. Am. Chem. Soc.* **2017**, 139, 17853.

[45] S. E. Renfrew and B. D. McCloskey, *ACS Appl. Energy Mater.* **2019**, 2, 3762.

[46] S. E. Renfrew, L. A. Kaufman and B. D. McCloskey, *ACS Appl. Mater. Interfaces* **2019**, 11, 34913.

[47] U.-H. Kim, H.-H. Ryu, J.-H. Kim, R. Mücke, P. Kaghazchi, C. S. Yoon and Y.-K. Sun, *Adv. Energy Mater.*, **2019**, 9, 1803902.

[48] H. H. Ryu, G. T. Park, C. S. Yoon and Y. K. Sun, *Small*, **2018**, 14, 1803179.

[49] D. Goonetilleke, N. Sharma, W. K. Pang, V. K. Peterson, R. Petibon, J. Li and J. R. Dahn, *Chem. Mater.*, **2018**, 31, 376.

[50] E. Flores, N. Vonrüti, P. Novák, U. Aschauer and E. J. Berg, *Chem. Mater.*, **2018**, 30, 4694.

[51] E. Flores, P. Novák, U. Aschauer and E. J. Berg, *Chem. Mater.*, **2019**, 32, 186.

[52] X. Liu, Z. Liang, Y. Xiang, M. Lin, Q. Li, Z. Liu, G. Zhong, R. Fu and Y. Yang, *Adv. Mater.*, **2021**, 33, 2005878.

[53] K. Märker, P. J. Reeves, C. Xu, K. J. Griffith and C. P. Grey, *Chem. Mater.*, **2019**, 31, 2545.

[54] M. Cotte, J. Susini, J. Dik and K. Janssens, *Acc. Chem. Res.* **2009,** 43, 705.

[55] H. Hu, J. Zhao, L. Wang, L. Shang, L. Cui, Y. Gao, B. Li and Y.-F. Li, *Trends Anal. Chem.* **2020**, 122, 115721.

[56] Y. Bi, J. Tao, Y. Wu, L. Li, Y. Xu, E. Hu, B. Wu, J. Hu, C. Wang, J.-G. Zhang, Y. Qi and J. Xiao, *Science*, **2020**, 370, 1313.

[57] J. Langdon and A. Manthiram, *Energy Storage Mater.*, **2021**, 37, 143.

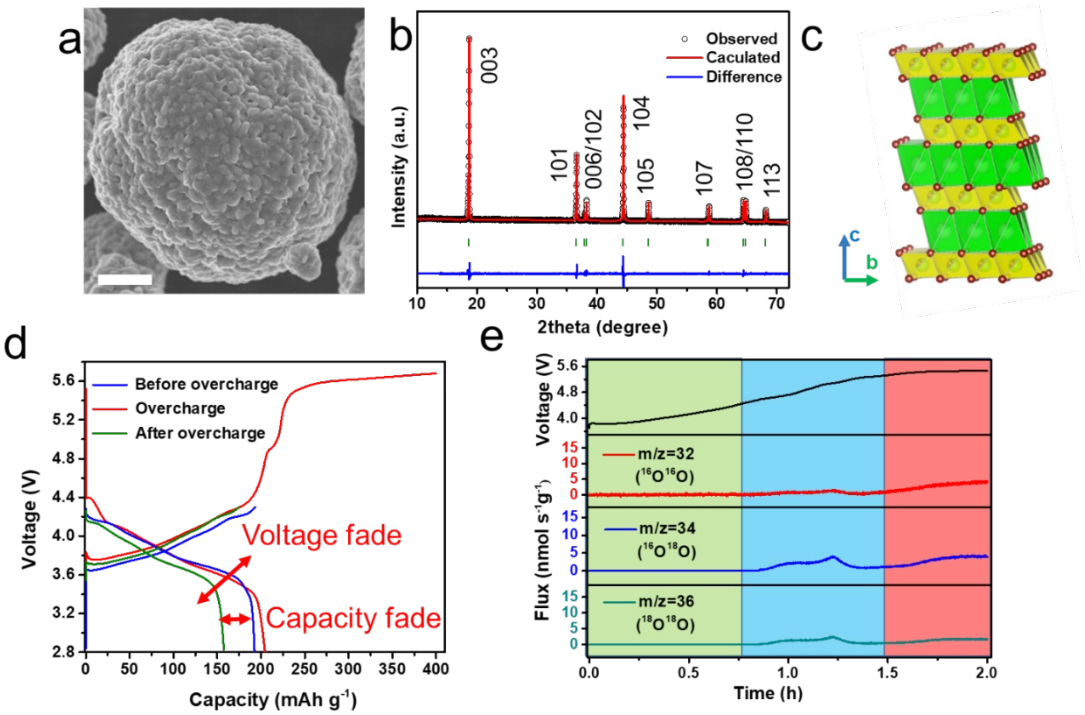

Figure 1 Structural properties of pristine NCM811 and oxygen release under overcharge. (a) SEM image, scale bar: 2 μm. (b) XRD pattern and (c) schematic of layered crystal structure; the red spheres represent oxygen ions, and the green and yellow octahedrons represent LiO_6 and TMO_6 units, respectively. (d) Charge–discharge curves before overcharge cycle (blue line), overcharge curve (red line) and after overcharge cycle (green line), and obvious electrochemical property degradation could be observed after this overcharge behavior. (e) OEMS results for O_2 evolution along overcharge process, and the distinction is based on ^{18}O labelled regions for that oxygen release. According to O_2 evolution case, the overcharge process could be divided into three stages (stage I, green; stage II, blue; stage III, red).

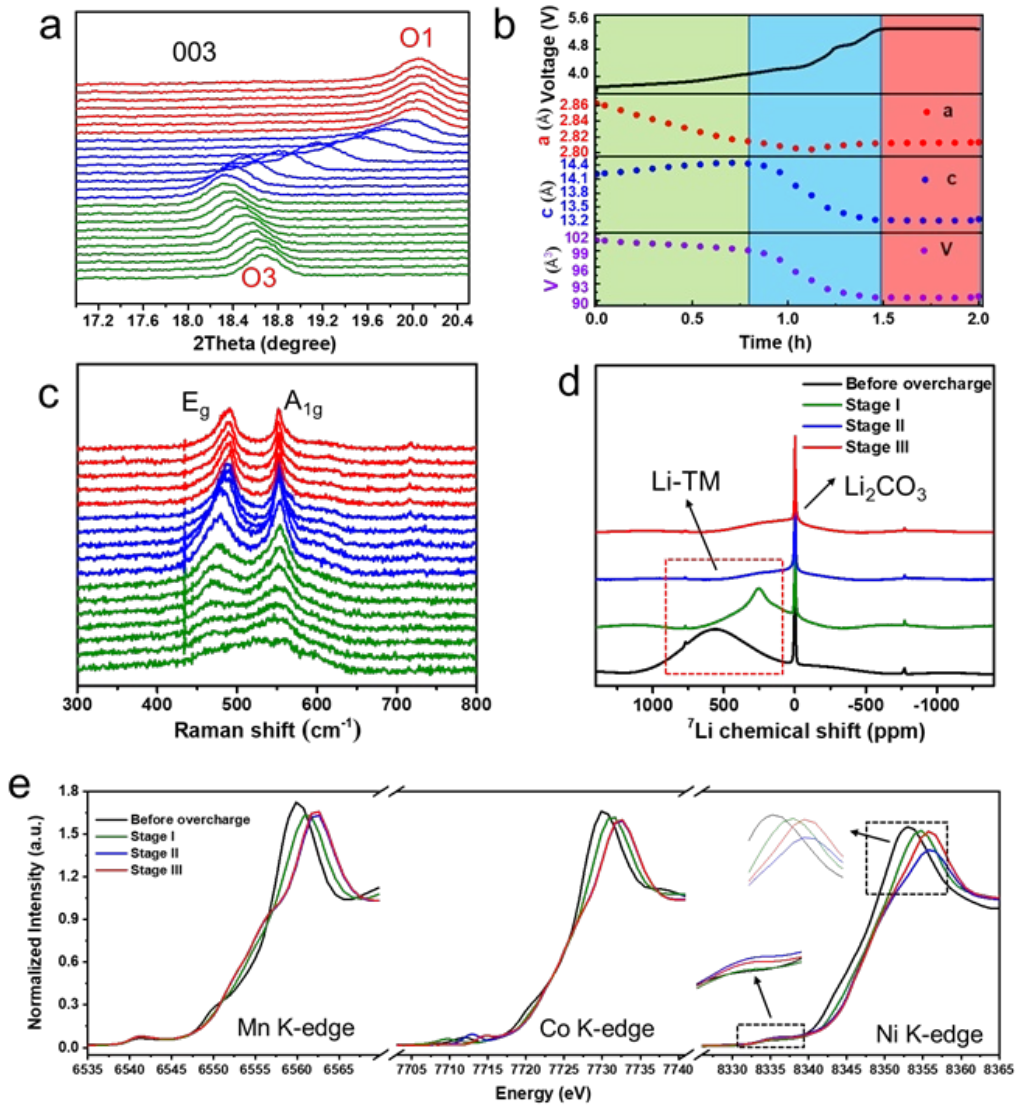

Figure 2 Revealing evolution of the bulk structure using in situ and ex situ diffraction/spectroscopy techniques. (a) In situ XRD scans in the range of 17°–20.6° and (b) related refinement crystal data for the whole overcharge process. The initial pattern could be indexed as the O3-type structure, and the later pattern could be indexed as the O1-type structure. No new phase appeared, even though strong crystal-lattice parameter variation occurred, especially for parameter c. (c) In situ Raman scans in the range of 300–800 cm^{-1} and (d) ex situ ^{7}Li ss-NMR scans at different stages. The green, blue, and red lines are related to stage I, II, and III, respectively. (e–g) Ni, Co, and Mn K-edge XANES scans for different stages. The arrow direction indicates the overall oxidation tendency for TMs during overcharge but Ni reduction in the later stage. For all the graphs, the black, green, blue, and red lines correspond to the pristine state and during/after stage I, II, and III, respectively.

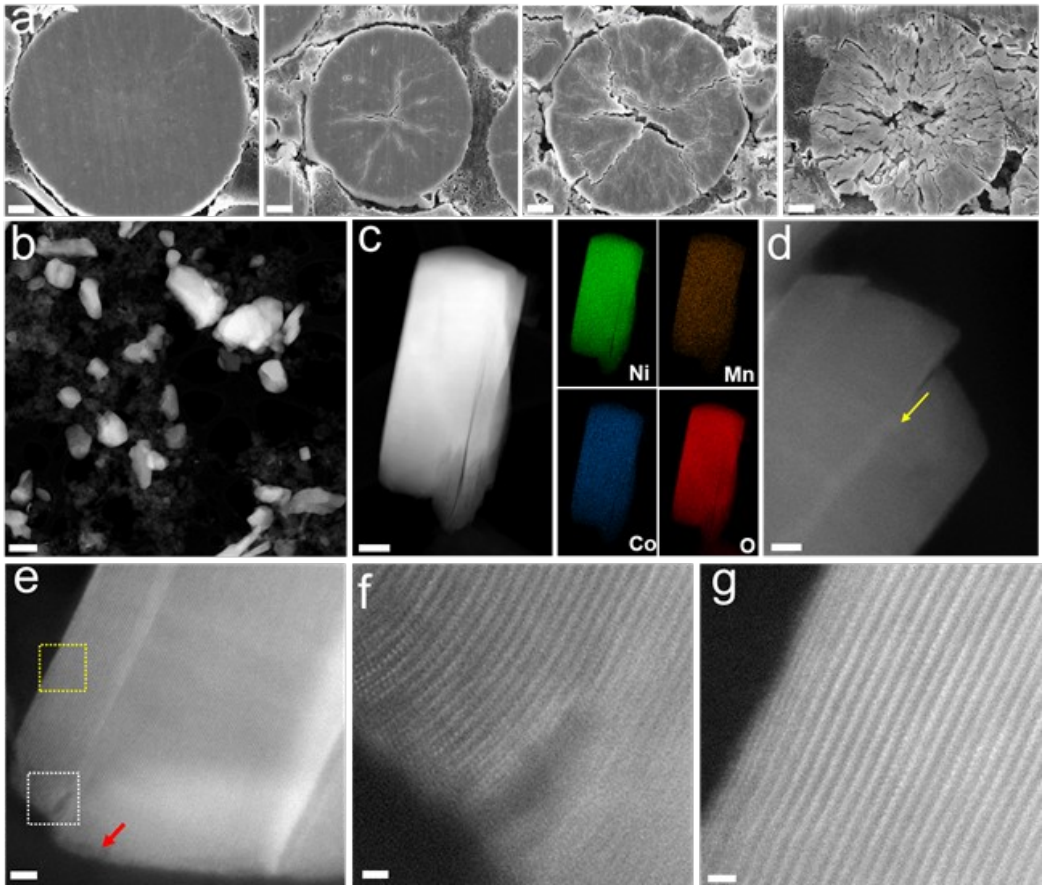

Figure 3 Spatial and temporal evolution of structural degradation of NCM811. (a) Cross-sectional SEM images showing the structural evolution during the overcharge process. (Images of the NCM811 after stage I, 4.7 V, stage II, and stage III are shown from left to right. (b) Representative HAADF-STEM image and the corresponding elemental maps of NCM811 after stage III. (d) HAADF-STEM image of NCM811 after the overcharge process. The yellow arrow indicates the gliding marks within the particle. (e–g) High-resolution STEM images of NCM811 after the overcharge process. Images of f and g correspond to the regions enclosed by the white and yellow squares in e, respectively. Scale bars: a 2 μm; b 500 nm; c 75 nm; d 10 nm; e 5 nm; f, g 1 nm.

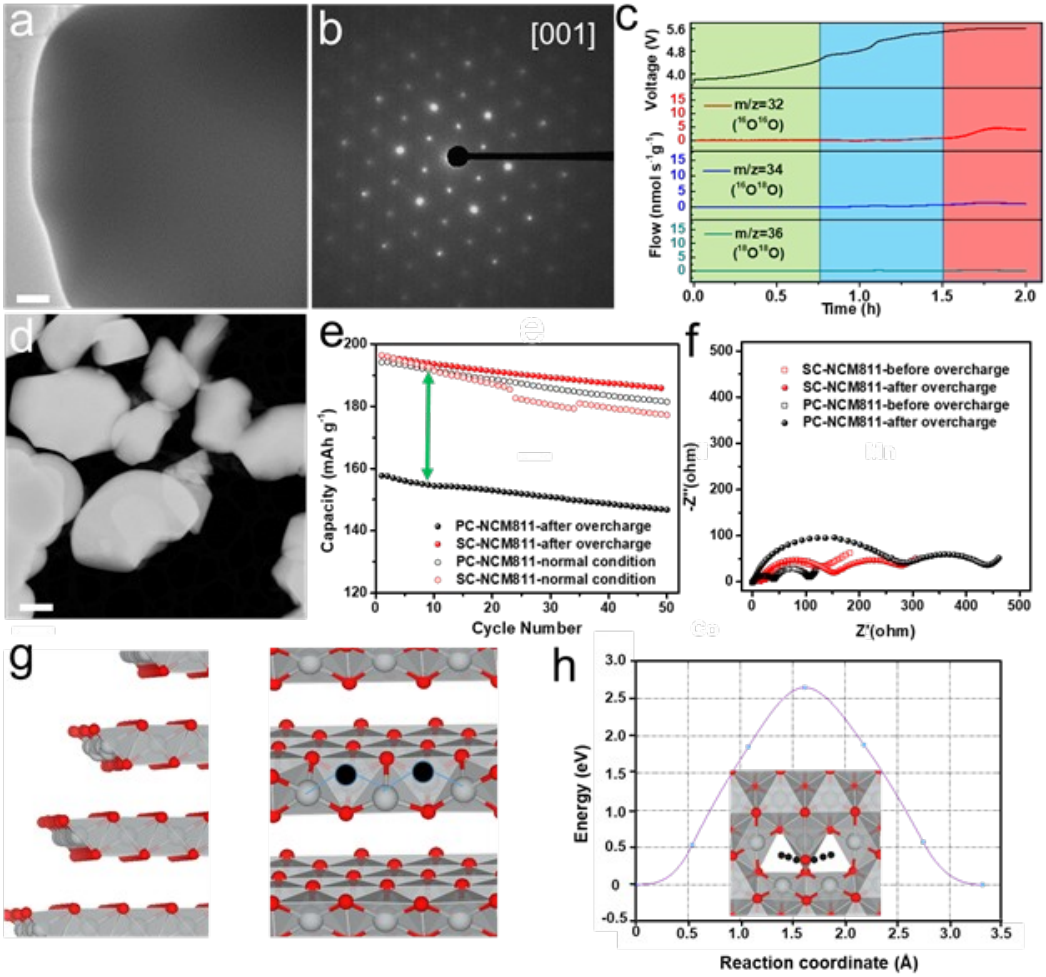

Figure 4 Structure characterization and oxygen-release behavior of single-crystalline NCM811. (a) TEM image of pristine SC-NCM811. (b) Electron diffraction pattern of a selected area of SC-NCM811 viewing along [001] direction. (c) $^{16}O^{16}O$ (m/z=32), $^{16}O^{18}O$ (m/z=34), and $^{18}O^{18}O$ (m/z=36) evolution during overcharge process. (d) Low-magnification HAADF-STEM image of SC-NCM811 after the overcharge process. (e) Cycling performance of two types of NCM811 under normal condition (solid sphere) and after the overcharge process (hollow spheres). (f) EIS data of two types of NCM811 before and after the overcharge process. (g) Side and top views of DFT optimized surfaces with two O vacancies at Li%=0.0. Black cycles indicate O vacancy. (h) Minimum energy path of O diffusing to a neighboring vacancy in the bulk at Li%=0.0. Black dots show the O positions along the path; the red one labels the saddle point. Scale bars: a 1 μm; d 1 μm.